FIRST RESULTS FROM THE SALSA AIRBORNE RE-ENTRY OBSERVATION CAMPAIGN

Clemens Mueller(1), David Leiser(1), Martin Eberhart(1), Stefanos Fasoulas(1), Stefan Loehle(1), Fabian Zander(2), Byrenn Birch(2), Ranjith Ravichandran(2), Gerad Armstrong(2), Juraj Toth(3), Tomas Paulech(3), Patrik Kaerraeng(4), Tobias Lips(4), Jiri Silha(5), Matej Zigo(5), Beatriz Jilete(6), Benjamin Bastida Virgili(6), and Stijn Lemmens(6)

(1)*HEFGiG, Institute of Space Systems, University of Stuttgart, 70569 Stuttgart, Germany,*
Email:muellerc@irs.uni-stuttgart.de
(2)*University of Southern Queensland, QLD 4350 Toowoomba, Australia*
(3)*Comenius University, 81499 Bratislava, Slovakia*
(4)*Hyperschalltechnologie Goettingen, 37120 Bovenden, Germany*
(5)*Astros Solutions s.r.o., 84248 Bratislava, Slovakia*
(6)*European Space Agency*

ABSTRACT

On September 8, 2024, the first of four CLUSTER-II satellites named *Salsa* re-entered the Earth's atmosphere approximately 2000 km west of Easter Island. The re-entry was the target of an airborne observation campaign conducted by an international team of scientists. Two hours before re-entry, the team took off aboard a Falcon 900 aircraft, equipped with 26 instruments distributed across six observation stations. This paper provides first results of the airborne observation campaign. Ten of the 26 instruments successfully detected the satellite for up to 20 seconds, with one infrared tracking camera capturing for even a longer time. The recorded intensity profiles reached their peak simultaneously at 18:47:10.7 UTC. Comparing this instant in time with the predicted fragmentation sequence, this bright flash corresponds to the main break-up event. Subsequently, there are three more flashes identified, which have led to the disintegration of the spacecraft.

Keywords: Airborne Observation, Cluster-II.

1. INTRODUCTION

After the operational phase of spacecraft such as satellites, the primary objective is their re-entry into the Earth's atmosphere to mitigate the accumulation of space debris [1]. Consequently, a rapidly increasing number of objects in space, especially in the Low Earth Orbit (LEO), will result in a respective increase in re-entry events [2]. Every event poses a potential ground risk for goods and people. Therefore, ensuring ground safety requires an improved understanding of the demise process, allowing for enhanced prediction tools to minimize the casualty risk.

The European Space Agency (ESA) coordinates the destructive re-entry research efforts through the *Clean Space Initiative* and *Design for Demise (D4D)* activities [3] in order to reach the international regulation requirements. The D4D activities intend to realize modified satellite structures to ensure complete demise during re-entry. This is supported by simulations using re-entry prediction tools and experimental ground testing [4]. However, only re-entry observations allow for the collection of real flight data on atmospheric entries. These data are crucial for validating numerical simulations and ground test facility testing. Due to the very remote locations of controlled re-entries, which are intentionally realized over uninhabited areas, airborne observation campaigns are deployed for re-entry observation over the ocean.

In the past, there have been several successful airborne observations. Three re-supply spacecraft for the International Space Station (ISS) have been observed over the South Pacific already: The European Automated Transfer Vehicle (ATV-1) in 2008 [5, 6], CYGNUS OA6 [7] ATK in 2016 and most recently CYGNUS-NG20 in July 2024 [8]. Furthermore, an unknown object named WT1190F was observed in 2015 [9]. Analysis of the data contributed to its identification as a trans-lunar injection stage from the 1998 Lunar Prospector mission [10]. The High Enthalpy Flow Diagnostic Group (HEFDiG) of the Institute of Space Systems (IRS) at the University of Stuttgart participated in all of these missions, as well as the University of Southern Queensland (UniSQ), except for the observation of ATV-1.

These missions provided valuable data and helped build necessary capabilities in this field of research. However, there is still a lack of flight data on destructive re-entries for the validation of prediction tools. The

Proc. 9th European Conference on Space Debris, Bonn, Germany, 1–4 April 2025, published by the ESA Space Debris Office
Editors: S. Lemmens, T. Flohrer & F. Schmitz, (http://conference.sdo.esoc.esa.int, April 2025)

four satellites of the Cluster-II mission offer the unprecedented opportunity to observe very similar re-entry events within a comparatively short time. Cluster-II was a mission designed to study the Earth's magnetosphere [11]. The highly eccentric orbit with an apogee of around 130000 km allows for a relatively accurate determination of the entry location and time, making it beneficial for airborne observation. Only the atmospheric density influences the behavior on the last orbit and thus the exact entry location. The re-entry of the Cluster-II satellite named *Salsa* took place on 8 September 2024 at 18:47 UTC over the South Pacific, approximately 2000 km west of Easter Island. The second satellite will re-enter the Earth's atmosphere in October 2025, followed by the last two satellites at the end of 2026.

As part of an ESA-coordinated effort, an international team conducted an airborne observation of the *Salsa* re-entry. The project was led by the Slovakian company ASTROS Solutions s.r.o., with numerical predictions provided by Hyperschalltechnologie Goettingen (HTG). The scientific strategy was led by HEFDiG, in collaboration with UniSQ and Comenius University Bratislava. UniSQ was responsible for the mission execution. The primary objective was to detect the main break-up event and its altitude. Most spacecraft that experience a controlled re-entry experience their main break-up at an altitude of 70-80 km [12]. The reason for this phenomenon is not yet fully understood. Additionally, the project aims to reconstruct the spacecraft's trajectory and analyze fragment dispersion including fragment identification, which is crucial for validating prediction tools. A major challenge was the entry during daylight: The bright sky made the use of spectroscopic systems with transmission gratings almost impossible since it produces continuous overlapping spectra.

The following sections provide an overview of the mission planning and execution phases. Additionally, the initial results of the observation campaign are presented.

2. MISSION PREPARATION

The observation campaign was preceded by a four-month preparation phase, which included numerical predictions, the definition of a scientific strategy and the organization of logistics.

2.1. Numerical simulations

HTG provided numerical simulations using their inhouse software SCARAB (Spacecraft Atmospheric Reentry and Aerothermal Break-up) based on trajectory predictions using orbital data from ESA. SCARAB is a spacecraft-oriented tool, meaning that the entire spacecraft is discretized in detail, and the analysis is conducted for the complete structure [13]. An accurate prediction of the entry time and location was needed to calculate a flight path for the aircraft that fulfilled the scientific objectives. During the last perigee pass before re-entry the spacecraft experienced significant deceleration due to the atmosphere. The uncertainty in the atmospheric density distribution caused a corresponding uncertainty in the drag force experienced by the spacecraft. Therefore, an accurate prediction to within a few seconds was only achievable after the last perigee pass, one orbital period (52 hours) before the actual re-entry. Figure 1 shows the latest prediction of the spacecraft's trajectory on-ground in geodetic coordinates starting at 120 km altitude. The satellite enters the atmosphere northwest of Easter Island and continues its trajectory westward. The blue crosses indicate predicted impact locations of surviving fragments.

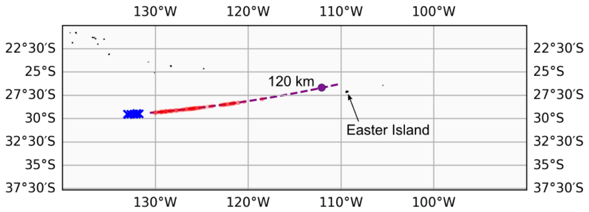

Figure 1: On-ground path of the re-entry trajectory of *Salsa* in geodetic coordinates.

The altitude of the fragments over time is depicted in Figure 2. The red curve represents the spacecraft's trajectory until fragments begin to form, after that, it marks the center of the fragment cloud. Fragment trajectories are shown in blue. It can be seen that the fragment cloud does not disperse significantly.

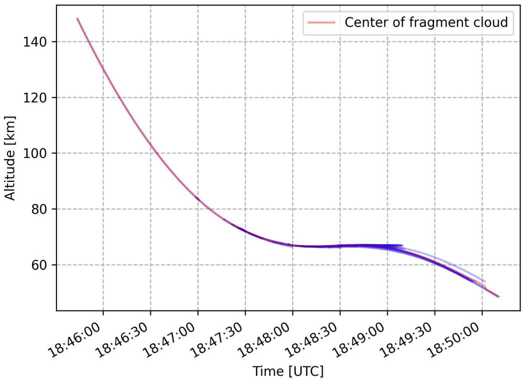

Figure 2: Fragment altitude over time.

The cluster satellites have a cylindrical shape with a diameter of 2.9 m and a height of 1.3 m [14]. Four antenna masts are mounted on the outside and the empty mass is about 550 kg. According to the prediction shown in Figure 2, the antennas will break off at an altitude of approx-

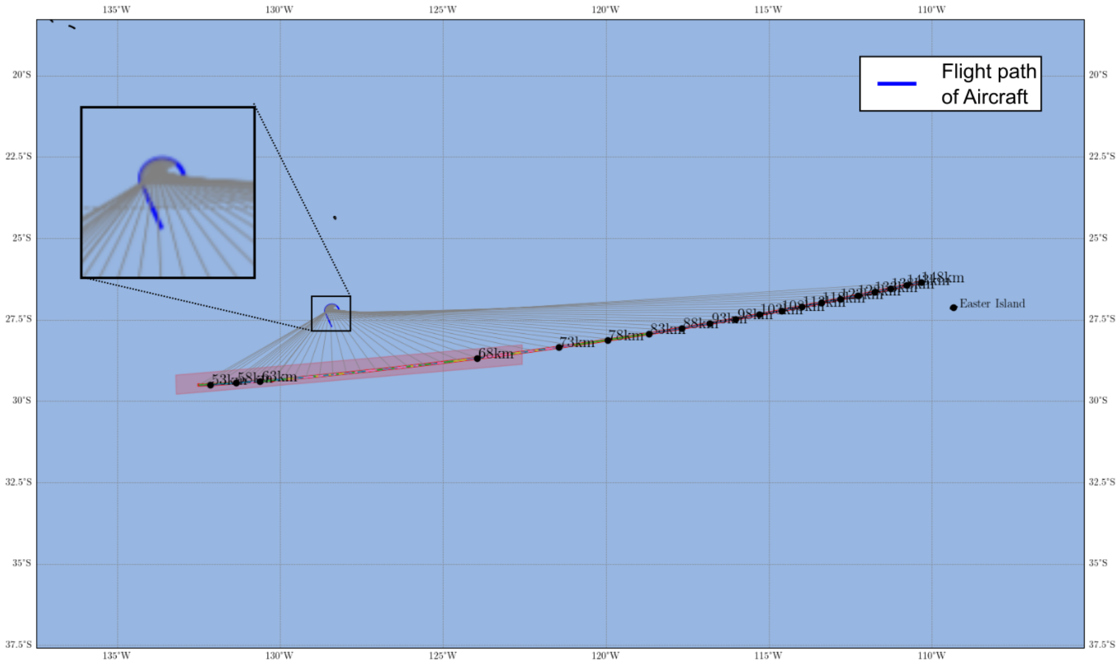

Figure 3: Determined aircraft flight path (blue curve). Numbers indicate the altitude of the satellite along the trajectory.

imately 82 km, followed by the main break-up at 78 km. The duration of the whole re-entry, starting from 120 km, is roughly four minutes. However, the satellite was expected to be visible during a significantly shorter period, in the order of one minute. Further details on the predictions can be found in [15].

2.2. Flight-path determination

The numerical simulations of the spacecraft trajectory are used to determine the flight path of the aircraft. Typically, the aircraft follows the trajectory by flying a turn with a constant bank angle, maximizing the section that remains within the field of view. Factors limiting the duration of the spacecraft visibility period are light intensity, which is affected by the distance between the aircraft and the spacecraft, the size of the optical window, and the aircraft bank angle. The turn's position is determined by the mission objectives, based on which part of the trajectory is of greatest interest. This requires a trade-off. When a specific event in the re-entry trajectory, such as the main break-up event, is of particular interest, the aircraft can be positioned closer to its predicted location. However, this increases the distance to the rest of the trajectory, potentially causing it to fall out of sight or become too weak to detect.

Figure 3 shows the flight path as determined for this observation campaign. The blue curve represents the flight path over ground, while the gray lines indicate the viewing direction toward the spacecraft at respective time points. The aircraft executes a clockwise turn north of the trajectory as the satellite passes the aircraft westwards. Since the re-entry occurs in the Southern Hemisphere and the local entry time is around noon, the sun is shining from the north. The flight path was optimized to capture the main break-up event while also focusing on the subsequent fragmentation process. This results in the closest distance to the spacecraft of about 270 km at an altitude of approximately 63 km.

Figure 4 shows the predicted viewing angles to the satellite during the mission, with the xy-plane of the aircraft and the center of the window as 0 degree elevation and azimuth. As a result, the aircraft's change in inclination at the beginning of the turn appears as a vertical line. For the observer, the satellite is slowly moving to the top left of the window reaching 70 km altitude. As the satellite passes the aircraft, it rapidly shifts toward the top right of the window. However, this curve does not reflect the temporal progression of the viewing angles.

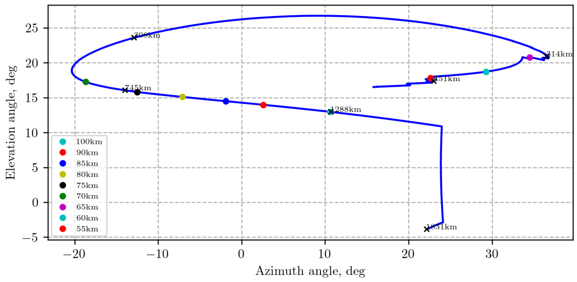

Figure 4: Predicted viewing angles in azimuth and elevation.

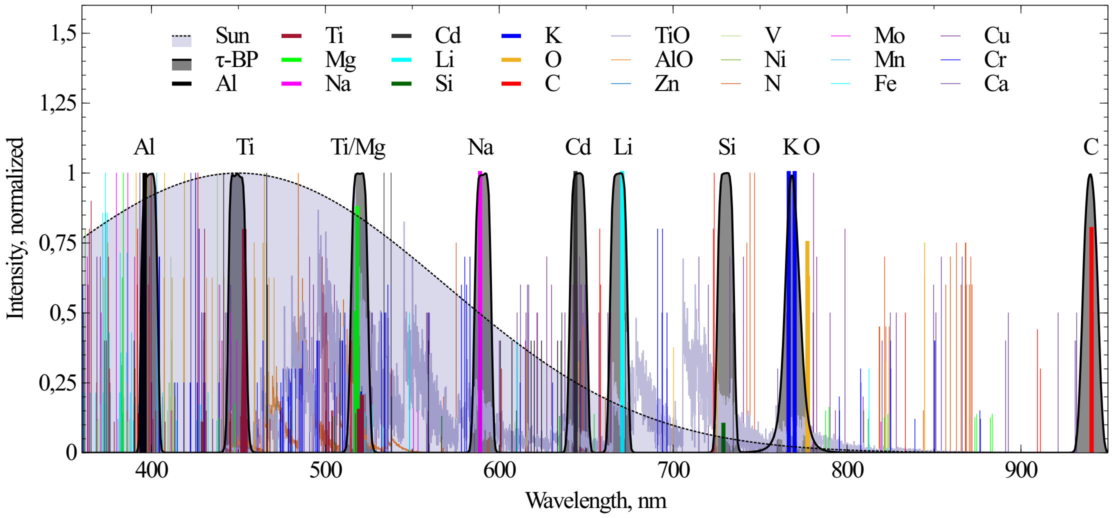

Figure 5: Normalized emission lines of the visible and near-infrared spectrum, Rayleigh-scattered sun spectrum and transmission curves of the selected bandpass filters.

2.3. Instrument selection

In general, the objectives were tackled by a combination of imaging cameras and spectrally resolving instruments to detect emission lines of relevant species. Figure 5 shows normalized emission lines of elements and molecules that could occur during the re-entry. These elements are mostly part of the satellite's material or the Earth's atmosphere. The thick lines represent the elements selected for detection: Aluminum, as the primary structural component, titanium for the fuel tanks, and carbon to detect fiber-reinforced plastic materials. Cadmium serves as a marker for the batteries, while oxygen, potassium and sodium are included due to their presence in the atmosphere and their frequent detection in prior observations. It was shown that the emission of lithium appears to be a spectral marker for the failure of the aluminum alloy Al 6060 and is therefore of major interest [16]. Silicon emission is an indicator for the early break-up phase as it is mainly part of the solar arrays. However, the team faced the severe challenge of observing under bright daylight conditions around local noon. This significantly impacted the feasibility of applying typical optical measurement techniques, such as spectroscopic imaging using cameras equipped with gratings. The background emission in the visible range, primarily due to Rayleigh-scattered sunlight (shown in Figure 5), leads to overlapping spectra, making spectral calibration extremely difficult. Entry slits can prevent this issue, but make object tracking extremely challenging. Instead, monochromatic cameras in combination with bandpass filters with a full width at half maximum (FWHM) of 10 nm were used to isolate single emission lines. This allows for the correlation of the intensity of a certain camera-filter combination to the abundance of the respective emission line. The transmission curves of the selected bandpass filters are depicted in Figure 5. A total of 26 instruments, distributed over six windows, were installed onboard the aircraft. Furthermore, a ground station (GS) was operated on Easter Island. The assignment of the instruments to the windows (stations), including their operator, is listed in Table 1. Three stations were operated by UniSQ, one by HEFDiG, and two by Comenius. Four of the six stations were manually tracked (t) and two remained static (s). An additional tracking camera was used for all tracked stations. Longpass filters were used to block the majority of the background radiation. Filter assignment was based on a trade-off between redundancy and independence amongst the stations, in case the recording or tracking of a station failed. Therefore, each station had at least one camera for pure imaging. The bandpass filters were assigned to ensure that the most relevant elements were detectable from at least two stations. In addition, three cameras equipped with transmission gratings and long pass filters were used in case the emission of the satellite would have been strong enough to record full spectra. A detailed list of all instruments can be found in [15].

All cameras run by a computer were connected to a GPS time server for accurate time synchronization. The remaining cameras were synchronized by an audio signal, generated by a microcomputer, and fed directly into the microphone input of the cameras. The microcomputer was synchronized using the time-server as well. This ensured that all systems were time-synchronized.

3. MISSION EXECUTION

The observation campaign started on the 8th of September 2024 from Easter Island. Figure 6 shows the top view of the aircraft, a Falcon 900, together with the assigned

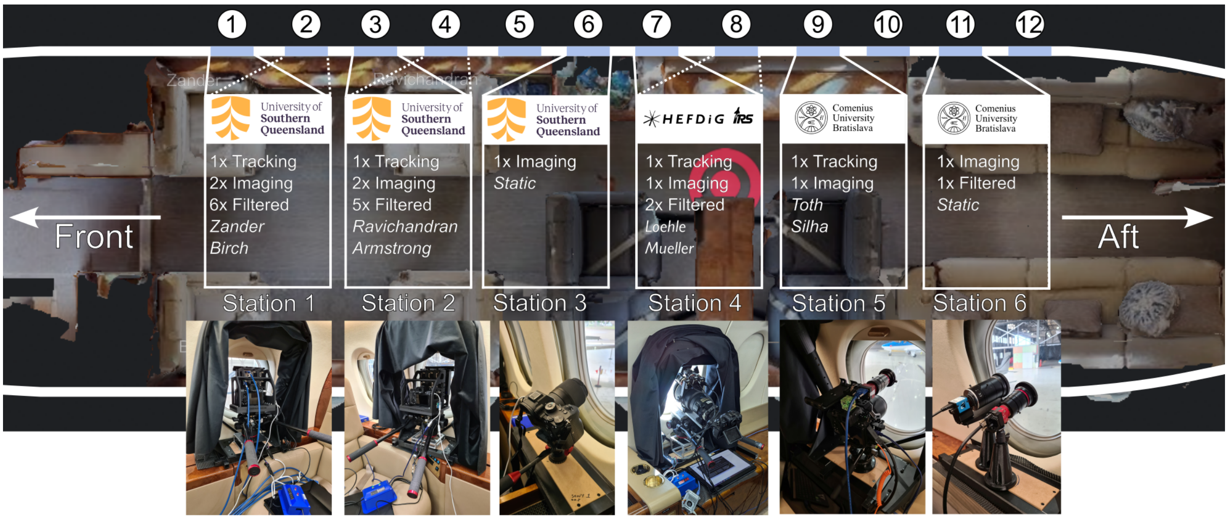

Figure 6: Top view of the aircraft with the assignment of the Stations.

Table 1: Overview of the flown instrument assignment during the mission.

Window	Operator	Instuments
1 (t)	UniSQ	2 x Imaging, Al-396 nm, Ti/Mg-520 nm, TiO-710 nm, Si-730 nm, O-777 nm, C-940 nm, Tracking,
2 (t)	UniSQ	2 x Imaging, Ti-450 nm, Na-590 nm, Cd-647 nm, Li-670 nm, Al-1310 nm, Tracking
3 (s)	UniSQ	Imaging
4 (t)	HEFDiG	Imaging, Li-670 nm Tracking, Grating-300 l/mm
5 (t)	Comenius	Imaging, Grating-500 l/mm
6 (s)	Comenius	K-770 nm, Grating-500 l/mm
GS (s)	Comenius	2 x Imaging

stations. All stations were enclosed with black curtains to eliminate window reflections. Each tracked station was operated by two scientists: one responsible for tracking and the other assisting in spacecraft detection and managing data handling. Stations 1, 2, and 4 were equipped with encoders to measure the viewing angle in azimuth and elevation. During the mission, the re-entering satellite was not directly observed by the operators. Therefore, the tracking was performed according to the predicted viewing angles shown in Figure 4.

4. RESULTS

The mission was executed as planned. Figure 7 shows an overlay of the planned flight path (see Fig. 3) and the flight path during the mission. The mission flight path deviated only slightly from the planned route. The turn was initiated slightly earlier, but it concluded at the same location as predicted. Figure 8 shows the viewing angles according to Figure 4. The red curve represents the predicted satellite position, considering the actual aircraft position and attitude during the mission. The green curve shows the pointing of the tracked station 2, which aligns closely with the predicted satellite position. This alignment is further supported by Figure 9, which illustrates the difference between the measured azimuth and elevation of stations 2 and 4 and the predicted satellite position. The dotted line indicates the field of view (FOV) of one of the cameras used. This demonstrates that the predicted satellite position remained well within the field of view during the time frame when the satellite was visible, shown as the vertical bar. In total, 10 out of 26 cameras onboard the aircraft successfully recorded the re-entry for up to 20 seconds. Four of the six stations had at

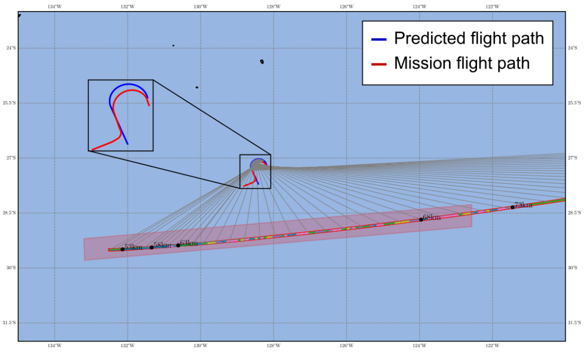

Figure 7: On-ground flight path during the mission.

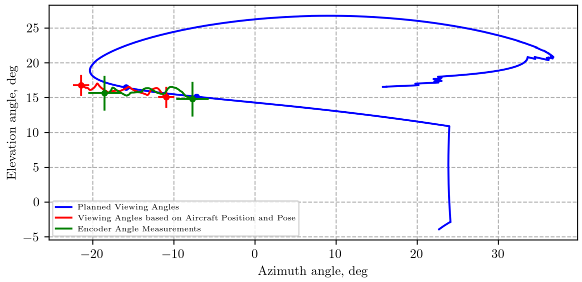

Figure 8: Viewing angles during the mission.

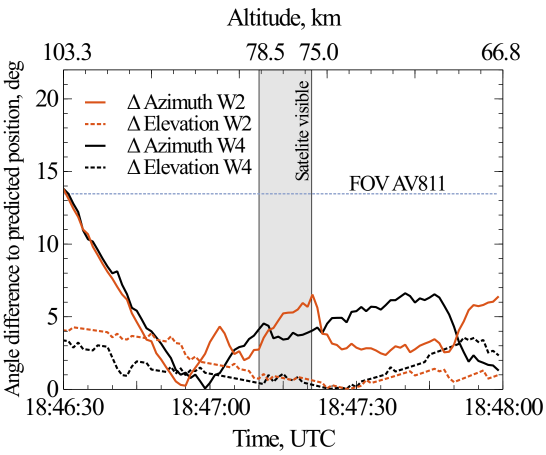

Figure 9: Viewing angle offset to the predicted position.

least one instrument that detected the satellite. Figure 10 shows the time frame in which the satellite was visible for 8 of the 10 cameras. The SWIR infrared tracking camera of station 2 detected the satellite for the longest time. This camera was equipped with an 850 nm longpass filter blocking the full visible wavelength range. The data shows that cameras that focused on short wavelength regions tend to detect the satellite for a shorter time, due to a stronger background from the blue sky. All instruments first detected the satellite at a similar time around 18:47:10 UTC.

Figure 11 shows intensity profiles of seven cameras, normalized to their maximum intensity. The left plot shows the profiles of three tracking cameras equipped with longpass filters. The right plot contains the profiles of cameras equipped with bandpass filters for element detection. All profiles reach their maximum at the same time at 18:47:10.7 UTC right after the satellite becomes visible. A time shift of 0.75 s was detected for the lithium-filtred camera at station 4. This is most probably an issue with the recording computer and has been corrected. Aside from the first peak, three more intensity peaks are visible in almost all profiles. These peaks are strong indicators of fragmentation events. Compared to the predictions (Figure 2) the timing of the first intensity peak aligns well with the predicted main break-up at approximately 80 km altitude. The exact times of the events are logged in table 2.

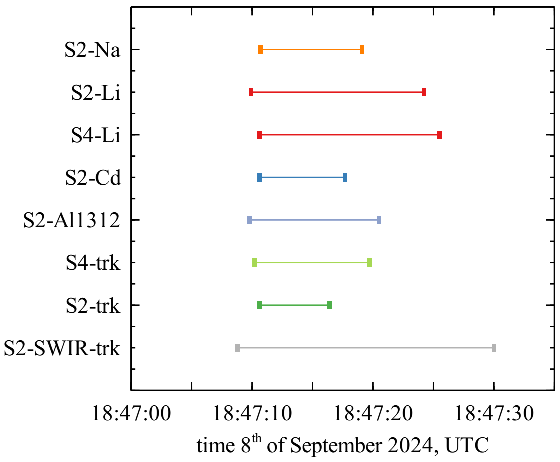

Figure 10: Time interval for each camera in which the satellite was detected [15].

Table 2: Event protocol.

Event No.	Time, UTC	Predicted Distance, km
1	18:47:10.72	917
2	18:47:12.55	900
3	18:47:15.15	870
4	18:47:16.30	860

Figure 12 shows images of the satellite at the four identified intensity peaks. The images show only the capsule, i.e. 41 x 41 pixel, and the contrast has been enhanced. The area that is observed by one single pixel at the distance of the lens to the object (i.e. aircraft to satellite) can be estimated by calculating the width and height of the pixel at this distance. The size W_p which one pixel covers at a given distance to the satellite D_{sat} can be approximated with:

$$W_p = \frac{W_{sensor} * D_{sat}}{f * N_{pixel}}. \tag{1}$$

where W_{sensor} is the sensor width, f the focal length of the camera lens and N_{pixel} the number of pixels in the respective dimension. Although this gives a simple estimate of the area a pixel covers, it neglects the optical system and its characteristics, which requires the analysis of the point spread function of the system. This simplified approach is used here for an initial interpretation of the captured images, only.

Taking the distances from Table 2, the length W_p for the SWIR camera results to 268 m to 285 m. For the AV 811

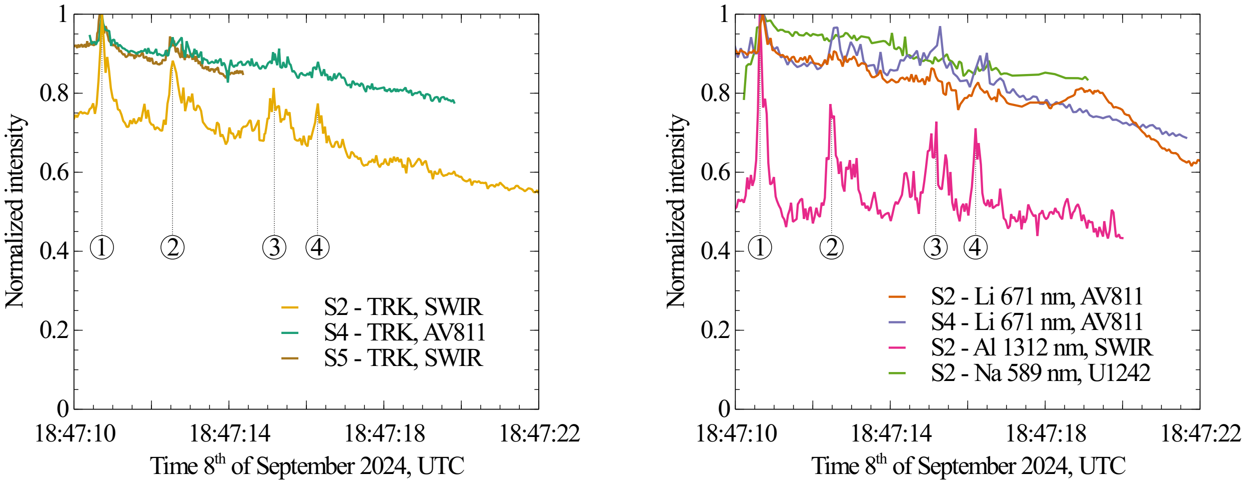

Figure 11: Normalized intensities over time for three cameras equipped with longpass filters for tracking (left) and four cameras equipped with bandpass filters for element detection (right).

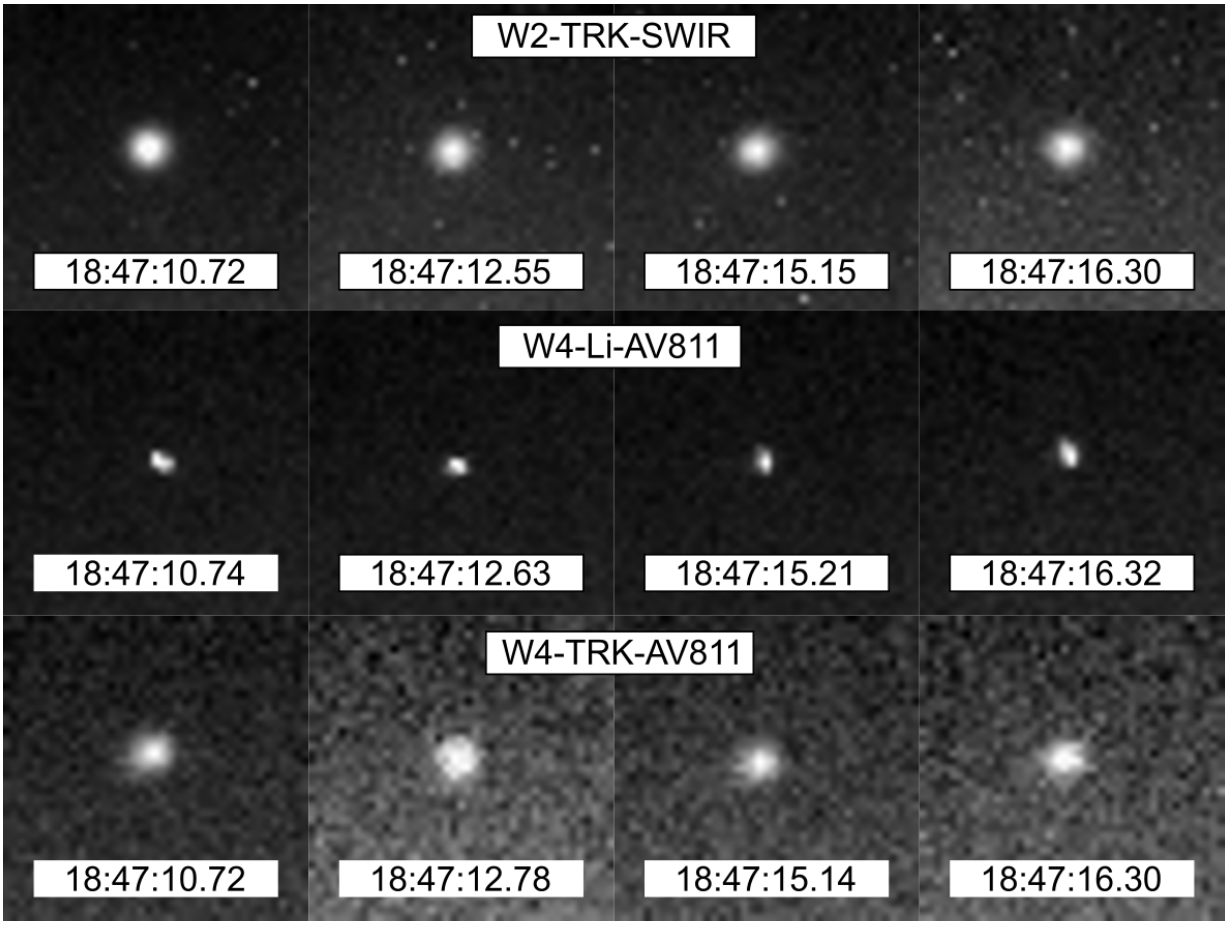

Figure 12: Image sequence of the satellite at the four intensity peaks for the SWIR tracking camera (top), the AV-811 lithium detecting camera (middle) and the AV-811 tracking camera (bottom).

camera setup, this results in a captured width of 153 m to 143 m. The change in shape of the bright spot might indicate also an orientation of the object. However, the view angle towards the satellite changes, because the aircraft is flying a continuous turn.

From 18:47:10 UTC to 18:47:20 UTC the satellite moved toward the aircraft reducing its distance from 900 km to 800 km. As a result, the viewing angle from the aircraft to the satellite is primarily from the front relative to its flight direction.

The first row displays frames captured by the infrared SWIR camera, which was used for tracking at station 2. In the first frame, the satellite appears as a single, symmetric, circular light source with an approximate diameter of seven pixels. Using Equation 1, this corresponds to a spatial extent of approximately 2 km. Compared to the following frames only the intensity decreases slightly, while the shape remains largely unchanged. The next row shows the frames of the AV 811 camera at station 4 which was equipped with a bandpass filter to detect lithium emission at 671 nm. Here, the satellite appears significantly smaller covering 3 to 4 pixels, corresponding to a spatial extent of approximately 600 m. Since the SWIR camera records over a broad spectral range in the near-infrared, a more extended signal is expected. In contrast to the SWIR images, minor changes in the signal shape are visible. In the first two images, the orientation is more horizontal and appears to be more vertical in the last two frames. The third row shows images of the AV 811 tracking camera at station 4 equipped with a long pass filter at 630 nm. The satellite has a width of five to six pixels and the shape compares well to the images of the SWIR camera. However, small features are visible on the left side, especially in the first and third frame. This is where, if visible, a trail of fragments would be expected.

5. CONCLUSION

This paper presents initial results of the airborne observation campaign for the observation of the re-entry of the Cluster-II satellite *Salsa*. The re-entry occurred at 12:46 Local Time Easter Island, which is bright daylight. The selected suite of instruments considered these challenging conditions. In total, 10 out of 26 instruments recorded usable data for up to 20 s. These 10 instruments were distributed over four of the six stations. A combination of cameras with long-pass filters for imaging and band-pass filters emission line selection was used, so that the scattered sunlight is blocked. The different element's emission was meant to identify occurring break-up events.

In this paper, the normalized intensity profiles are plotted and show the presence of four distinct peaks, with the first peak being the maximum across all instruments. Only after calibration for absolute radiance, these emissions can be compared and eventually distinguished from potential continuum radiation of the spacecraft.

The time of the occurring intensity peaks was compared to numerical predictions of the fragmentation sequence. This leads to the conclusion that the first peak corresponds to the main break-up event predicted to occurr at an altitude of approximately 80 km. This aligns with the observed break-up corridor of 80-70 km altitude for large spacecraft. The three subsequent intensity peaks are supposed to correspond to additional fragmentation events. In the images, the satellite appears as a circular light source covering 3 to 7 pixels in diameter. The shape of the satellite does not change significantly across the four intensity peaks.

Although the object appeared as a faint dot in the observation data, a successful detection of the fragmentation, particularly the main break-up has been successfully realized. Given that three more Cluster-II satellites are expected to re-enter in 2025 and 2026, this study strongly suggests their observation.

ACKNOWLEDGMENTS

The authors sincerely appreciate the outstanding cooperation with Falcon-Air. Their team, especially the pilots, supported us at all times, ensuring the success of the mission. This work is funded through the ESA contract No.4000145029/24/D/MRP.

REFERENCES

1. L. Innocenti. Esa clean space initiative.
2. ESA Space Debris Office. Esa's annual space debris environmental report.
3. Dive - guidelines for analysing and testing the demise of man made space objects during re-entry.
4. D. Leiser, F. Zander, S. Loehle, D. R. Buttsworth, and R. Choudhury. Determining reentry breakup forces in an impulse facility. In *4th International Workshop on Space Debris Re-entry*, Darmstadt, Germany, 2018. ESA ESOC.
5. S. Loehle, R. Wernitz, G. Herdrich, M. Fertig, H.-P. Röser, and H. Ritter. Airborne re-entry observation experiment slit: Uv spectroscopy during stardust and atv1 re-entry. *CEAS Space Journal*, 1(1), 2010. ISSN 1868-2502. doi: 10.1007/s12567-010-0005-3.
6. J. B. Snively, M. J. Taylor, and P. Jenniskens. Airborne imaging and nir spectroscopy of the esa atv spacecraft re-entry: Instrument design and preliminary data description. *International Journal of Remote Sensing*, 32(11):3019–3027, 2011. doi: 10.1080/01431161.2010.541516.
7. S. Loehle, F. Zander, S. Lemmens, and H. Krag. Airborne observations of re-entry break-up: Results and prospects. In *7th European Conference on Space Debris*, Darmstadt, Germany, 2017.

8. D. Leiser, C. Mueller, M. Eberhart, S. Loehle, G. Armstrong, B. Birch, A. Lock, R. Ravichandran, F. Zander, S. Poovathingal, and A. Martin. Early entry analysis of cygnus ng-20. In *9th Space Debris Conference*. 2025.
9. P. Jenniskens, J. Albers, M. Koop, M. Odeh, K. Al-Noimy, K. Al-Remeithi, K. Al Hasmi, R. F. Dantowitz, F. Gasdia, S. Loehle, F. Zander, T. Hermann, D. Farnocchia, S. R. Chesley, P. W. Chodas, R. S. Park, J. D. Giorgini, W. J. Gray, D. K. Robertson, and T. Lips. Airborne observations of an asteroid entry for high fidelity modeling: Space debris object wt1190f. In *54th AIAA Aerospace Sciences Meeting*, AIAA SciTech Forum, Reston, VA, USA, 2016. AIAA American Institute of Aeronautics and Astronautics. doi: 10.2514/6.2016-0999.
10. Traci Watson. Falling space debris traced to 1998 lunar mission. *Nature*, 2016. ISSN 1476-4687. doi: 10.1038/nature.2016.19162.
11. C. P. Escoubet, M. Fehringer, and M. Goldstein. The cluster mission. *Annales Geophysicae*, 19(10/12): 1197–1200, 2001. ISSN 0992-7689. doi: 10.5194/angeo-19-1197-2001.
12. C. Mueller, D. Leiser, S. Loehle, and S. Fasoulas. Transient plasma wind tunnel testing under thermomechanical loads for reentry break-up analysis. *AIAA Journal of Spacecraft and Rockets*, pages 1–8, 2024. doi: 10.2514/1.A36039.
13. T. Lips and B. Fritsche. A comparison of commonly used re-entry analysis tools. *Acta Astronautica*, 57(2-8):312–323, 2005. ISSN 0094-5765. doi: 10.1016/j.actaastro.2005.03.010.
14. S. Lemmens, K. Merz, Funke Q., B. Bonvoisin, S. Loehle, and H. Simon. Planned yet uncontrolled re-entries of the cluster-ii spacecraft. In *7th European Conference on Space Debris*, Darmstadt, Germany, 2017. URL `https://conference.sdo.esoc.esa.int/proceedings/sdc7/paper/647/sdc7-paper647.pdf`.
15. S. Loehle, F. Zander, P. Kaerraeng, T. Lips, G. Armstrong, B. Birch, R. Ravichandran, C. Mueller, J. Toth, T. Paulech, J. Silha, B. Jilete, and S. Lemmens. Design and execution of the airborne re-entry observation campaign of the cluster-ii salsa re-entry: under review. *CEAS Space Journal*, 2025. ISSN 1868-2510.
16. D. Leiser, S. Loehle, and S. Fasoulas. Spectral features for re-entry break-up event identification. *Journal of Spacecraft and Rockets*, 59(5):1496–1506, 2022. ISSN 0022-4650. doi: 10.2514/1.A35258.